Journal of Materials Chemistry A
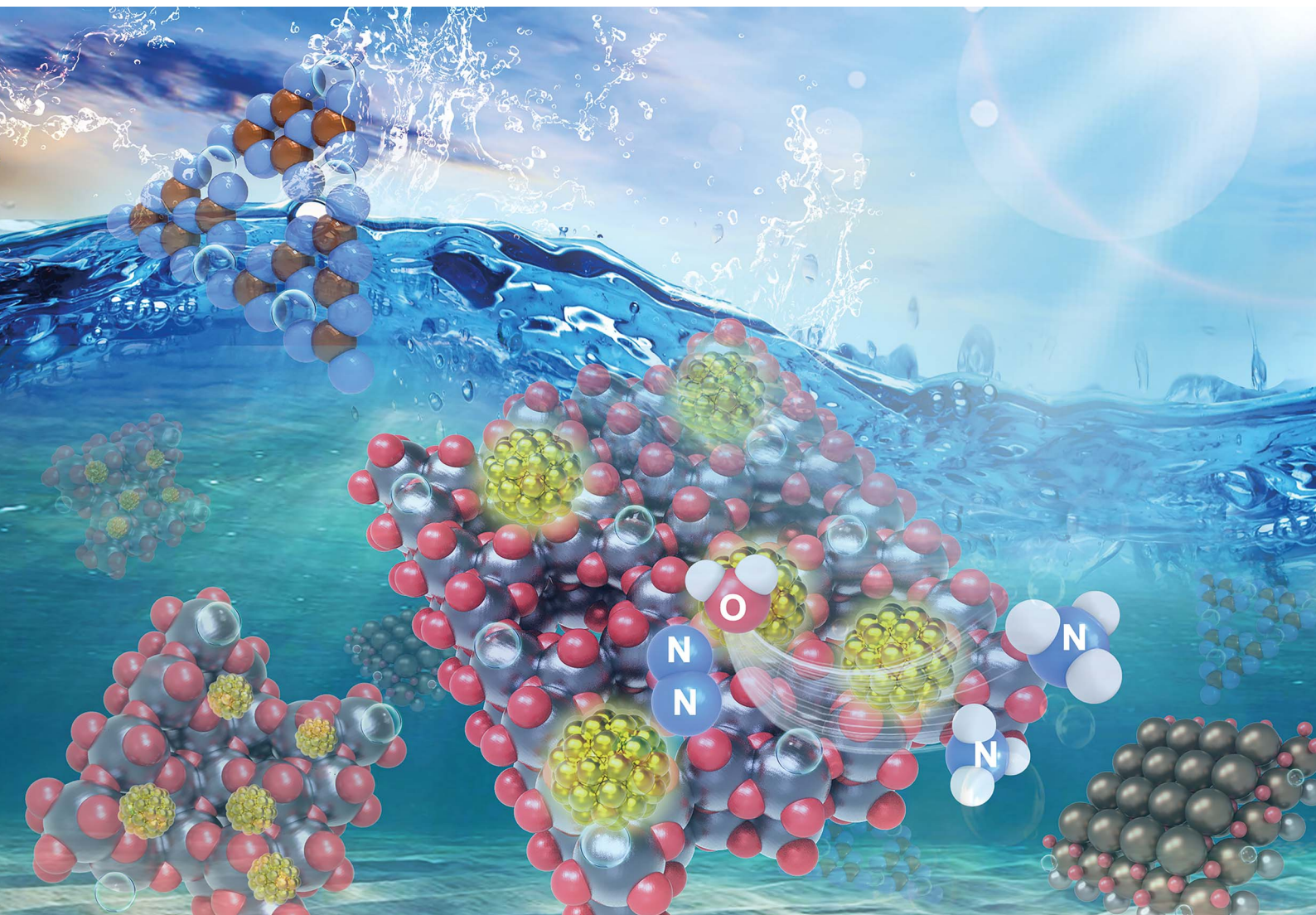
Materials for energy and sustainability

rsc.li/materials-a

Themed issue: Emerging Investigators 2021

ROYAL SOCIETY
OF CHEMISTRY

PERSPECTIVE
Jingrun Ran, Shi-Zhang Qiao *et al.*
Two-dimensional building blocks for photocatalytic
ammonia production

Check for updates

Two-dimensional building blocks for photocatalytic ammonia production

Jingrun Ran, [ID] * Bingquan Xia, Yanzhao Zhang and Shi-Zhang Qiao [ID] *

Owing to its extensive utilization in fertilizer generation and as an energy carrier, ammonia (NH_3) is deemed to be one of the most essential chemicals. Currently, NH_3 generation mostly depends on the Haber–Bosch approach under harsh conditions, resulting in tremendous energy usage and environmental problems. Photocatalytic NH_3 generation represents a clean, inexpensive and environmentally friendly method to transform water and nitrogen into ammonia utilizing sunlight under ambient conditions. Recently, two-dimensional (2D) building blocks have received great attention in the photocatalysis field thanks to their outstanding features of high surface area, plentiful reactive sites, ultrathin thickness and short charge-to-surface transfer distance. This perspective summarizes the design and synthesis of photocatalysts prepared utilizing 2D building blocks towards light-driven NH_3 production. Our contribution highlights the in-depth and comprehensive structure/composition–performance relationship in 2D building block based photocatalysts for light-induced NH_3 production. We also discuss the delicate and insightful reaction mechanisms in 2D building block based photocatalytic NH_3 production. Finally, we propose the possible opportunities in merging advanced characterization techniques as well as powerful theoretical computations towards the rational design and fabrication of high-performance 2D material based photocatalysts towards light-induced NH_3 generation.

1. Introduction

As a pivotal feedstock for synthesizing fertilizers and an important energy carrier, ammonia (NH_3) is produced in an amount of *ca.* 150 million tons annually worldwide.[1–23] Presently, industrial-scale preparation of NH_3 still depends upon the conventional Haber–Bosch approach developed in the early 1900s. But this Haber–Bosch process is performed under harsh conditions: elevated temperature (350–550 °C) together with high pressure (150–350 atmosphere pressure) using iron-based catalysts, which utilizes *ca.* ~1% of global energy supply and large amounts of fossil fuels to produce hydrogen (H_2) as a feedstock.[1–23] Hence, the development of a sustainable and environmentally benign strategy to produce NH_3 is of paramount significance.

School of Chemical Engineering and Advanced Materials, The University of Adelaide, Adelaide, SA 5005, Australia. E-mail: s.qiao@adelaide.edu.au; Jingrun.ran@adelaide.edu.au

Dr Jingrun Ran received his BE and ME degrees in Materials Science and Engineering from Wuhan University of Technology, and PhD degree in Chemical Engineering from the University of Adelaide. Now he is working as an ARC DECRA Fellow in Prof. Shi-Zhang Qiao's group, focusing on the atomic-level design and synthesis of photocatalysts for producing energy fuels and value-added chemicals using renewable solar energy. Dr Jingrun Ran has been recognized as a Clarivate Highly Cited Researcher in 2020.

Mr Bingquan Xia received his Master's degree in chemistry after graduating from Wuhan University in 2016. He is currently a PhD candidate under the supervision of Prof. Shi-Zhang Qiao at the University of Adelaide. His research is focused on the development of highly efficient photocatalysts for solar energy conversion.

Photocatalytic NH_3 production is a clean, cost-effective, and eco-friendly technique capable of converting nitrogen (N_2) and water (H_2O) into NH_3 using renewable solar energy at room temperature and under atmospheric pressure.[24–51] To realize industrial-scale photocatalytic NH_3 production, the core target is the exploration of highly active, strongly reliable and inexpensive nanostructured materials. Recently, two-dimensional (2D) materials have garnered tremendous attention in a variety of fields (*e.g.*, electronics, catalysis and optoelectronics) ever since the discovery of graphene.[24–63] Their distinctive features of high surface area, abundant reactive centres, ultrathin thickness and short bulk-to-surface distance make them outstanding building blocks to construct high-performance photocatalysts.

A range of 2D building blocks, *e.g.*, graphitic carbon nitride (g-C_3N_4),[24–27] BiOCl,[30] Bi_3O_4Br,[31] BiOBr,[32] layered double hydroxides (LDHs),[33–35] TiO_2,[36] MoS_2,[38] and SmOCl,[39] have been developed as single-component 2D photocatalysts for NH_3 production. Accordingly, a variety of strategies, *e.g.*, elemental doping,[27,30,33,35,36] creating vacancies,[24,25,27,30–37,39] modification on the termination,[24,26] producing porosity,[24,27] and/or crystal facet engineering,[30,32] have been adopted to tailor the physicochemical characteristics of the above 2D building blocks for achieving enhanced activity, selectivity and stability in photocatalytic NH_3 generation. Besides, heterojunctions based on 2D building blocks have also been designed and prepared for light-driven NH_3 production. A series of binary heterojunctions, *i.e.*, zero-dimensional (0D)/2D,[40–46] 2D/2D[47,48] and three-dimensional (3D)/2D,[49] as well as ternary heterostructures[50,51] have been explored as efficient, highly selective and robust photocatalysts towards light-induced generation of NH_3.

In this perspective, we for the first time summarize all the photocatalysts synthesized utilizing 2D building blocks towards photocatalytic NH_3 production. The in-depth and overall structure/composition–performance relationship in these 2D building block based photocatalysts is discussed. Additionally, the insightful and delicate reaction mechanisms in photocatalytic NH_3 production are also explained. Finally, we propose the possible opportunities in this research field with special focus on merging the advanced characterization techniques, *e.g.*, aberration-corrected scanning transmission electron microscopy (AC-STEM), synchrotron-based X-ray absorption spectroscopy (XAS), *in situ* Raman, and *in situ* Fourier transform infrared (FTIR) spectroscopy, and powerful theoretical calculations, to develop high-performance photocatalysts based on 2D building blocks for NH_3 generation.

2. Merits of 2D building blocks in photocatalytic NH_3 production

The distinct physicochemical features of 2D building blocks endow them with many outstanding merits in photocatalytic NH_3 production:[24–51] (i) their large surface area and abundant reactive sites facilitate the adsorption/activation/reduction of N_2 into NH_3; (ii) their ultrathin thickness benefits the dissociation and migration of photo-induced charge carriers from the bulk onto the surface; (iii) their large surface area facilitates the formation of electronic coupling with other materials for efficient interfacial charge carrier separation and migration; (iv) their tailorable thickness allows the alteration of band gap width *via* the quantum confinement effect, accompanied by modulation of light absorption capacity and conduction/valence band edge positions; (v) their highly exposed surface atoms also facilitate the adoption of various engineering strategies (*e.g.*, doping, creating vacancies and single-atom anchoring) to acquire the desired properties and functions.

It should be noted that various types of active sites, *e.g.*, cation/anion vacancies,[25,27,30,31,33–37,39,42,45] incorporated heteroatoms,[35,49] and anchored single atoms,[32,40,41] have been developed on 2D material based photocatalysts for efficient

Yanzhao Zhang received his BE degree from Wuhan University and ME degree in Materials Science and Engineering from Zhejiang University, and is now a PhD candidate under the supervision of Prof. Shi-Zhang Qiao and Dr Jingrun Ran at the University of Adelaide. Presently, Yanzhao is working on photocatalytic CO_2 conversion.

Shi-Zhang Qiao received his PhD degree in chemical engineering from the Hong Kong University of Science and Technology in 2000, and is currently a Chair Professor at the School of Chemical Engineering and Advanced Materials at the University of Adelaide, Australia. His research expertise is in nanomaterials for new energy technologies. He has co-authored more than 430 papers in refereed journals with over 73 000 citations and an h-index of 141. In recognition of his achievements in research, he was honoured with the prestigious ARC Laureate Fellow (2017), Exxon-Mobil Award (2016), ARC Discovery Outstanding Researcher Award (2013), and the Emerging Researcher Award (2013, the ENFL Division of the American Chemical Society).

Table 1 Single-component 2D photocatalysts for NH_3 production

Photocatalyst	Synthesis method	Light source	Reactant solution	Activity (μmol h^{-1} g^{-1})	Quantum efficiency (%)	Stability	Detection method	References (year)
Porous g-C$_3$N$_4$ with nitrogen vacancies and cyano groups	Alkali-assisted heat treatment	Simulated solar light (AM 1.5G, 100 mW cm^{-2})	20 v% methanol aqueous solution	1590			Nessler's reagent	24 (2019)
g-C$_3$N$_4$ with carbon vacancies	High-temperature peeling method	Xe lamp	Water	84		>100 min	Nessler's reagent	25 (2019)
g-C$_3$N$_4$ with cyano groups and intercalated K$^+$	KOH-assisted calcination and ultrasonication	Xe lamp (λ > 400 nm)	Ethylene glycol	3420		>4 hours	Nessler's reagent	26 (2019)
S doped g-C$_3$N$_4$ with C vacancies	Thermal polymerization of thiourea	Xe lamp	4 v% methanol aqueous solution	5990		>4 hours	Nessler's reagent	27 (2018)
BiOCl with Br doping and O vacancies	Surfactant assisted solvothermal approach	Xe lamp (λ > 400 nm)	Deionized water	126		>5 hours	Nessler's reagent	30 (2019)
Bi$_3$O$_4$Br with Bi and O vacancies	Surfactant assisted self-assembly strategy	Xe lamp	Distilled water	50.8		>4 hours	Nessler's reagent	31 (2019)
BiOBr with O vacancies	Surfactant assisted hydrothermal approach	Xe lamp	Deionized water	54.7		>12 hours	Nessler's reagent	32 (2018)
CuCr LDH with O vacancies and doped Cu^{2+} ions	Co-precipitation method	Xe lamp (λ > 400 nm)	Double distilled water	57.1	0.10 at 500 nm	>5 hours	Nessler's reagent	33 (2017)
ZnCr LDH with oxygen and cation vacancies	Alkali-etching and hydrothermal approach	Xe lamp	Ultra-pure water	33.19	0.95 at 380 nm, 0.34 at 420 nm, 0.11 at 550 nm	>5 hours	Indophenol blue method	34 (2020)
ZnAl LDH with O vacancies and doped Cu$^{\delta+}$	Co-precipitation approach	Xe lamp	Ultra-pure water	110	1.77 at 265 nm, 0.56 at 365 nm	>40 hours	Indophenol blue method	35 (2020)
TiO$_2$ with O vacancies and doped Cu	Hydrothermal approach	Xe lamp	Ultra-pure water	78.9	0.08 at 600 nm, 0.05 at 700 nm	>5 hours	Indophenol blue method	36 (2019)
MoO$_{3-x}$ with O vacancies	Hydrothermal approach	Xe lamp	Distilled water	1.11	0.013 at 365 nm	>24 hours	Ion chromatography	37 (2019)
MoS$_2$	Hydrothermal approach	Xe lamp (λ > 420 nm)	Deionized water	325		>10 hours	Indophenol blue method	38 (2017)
SmOCl with O vacancies	Wet-chemical method using graphene oxide as the template	Xe lamp	Deionized water	426	0.32 at 420 nm	>4 hours	Nessler's reagent	39 (2019)

This journal is © The Royal Society of Chemistry 2021

J. Mater. Chem. A, 2021, **9**, 18733–18745 | **18735**

adsorption, activation and reduction of N_2 to produce NH_3. Each of the above types alone or two types of active sites together could apparently promote the adsorption/activation/reduction of N_2 molecules, as confirmed by experimental characterization, *e.g.*, N_2 temperature-programmed desorption (TPD) and/or theoretical computations, thus leading to apparently improved activity and selectivity in photocatalytic N_2-to-NH_3 conversion.

3. Single-component 2D photocatalysts

Up to now, various single-component 2D photocatalysts have been developed and utilized in photocatalytic NH_3 generation (see Table 1).[24–27,30–39] A series of approaches, *e.g.*, heteroatom incorporation, generation of vacancies, morphology control and surface modifications, have been explored to engineer the properties of these single-component 2D photocatalysts for highly efficient, highly selective and steady light-driven NH_3 generation. They are classified into four categories: (1) g-C_3N_4 based 2D photocatalysts;[24–27] (2) bismuth based 2D photocatalysts;[30–32] (3) LDH based 2D photocatalysts;[33–35] and (4) other 2D photocatalysts,[36–39] which are introduced in detail as follows.

3.1 g-C_3N_4 based 2D photocatalysts

In recent years, g-C_3N_4 has attracted enormous attention in the photocatalysis field thanks to its appealing properties of appropriate band gap width, favourable band edge positions, reliable stability, earth abundance and excellent processability.[24–27,62,63] Particularly, several g-C_3N_4 based 2D photocatalysts are designed and prepared towards photocatalytic NH_3 generation.[24–27] Various techniques, including elemental doping,[27] vacancy defect creation,[24,25,27] terminal modification[24,26] and/or porosity generation,[24,27] have been applied to engineer the physicochemical characteristics and optimize the photocatalytic NH_3 production performance of 2D g-C_3N_4.

Xue *et al.*[24] reported the synthesis of porous g-C_3N_4 nanosheets with cyano groups and nitrogen defects by alkali-assisted calcination of urea. The as-prepared porous g-C_3N_4 nanosheets with cyano groups and nitrogen defects present an enhanced photocatalytic N_2 fixation rate of 1590 μmol h^{-1} g^{-1} in comparison to pure g-C_3N_4 without any co-catalyst under simulated solar irradiation (AM 1.5G). The elevated photocatalytic activity is caused by the synergistic impacts of strengthened light harvesting, advanced photo-induced charge carrier migration and adsorption of N_2 gas molecules. In another study, Zhang *et al.*[25] synthesized ultrathin g-C_3N_4 nanosheets with abundant carbon vacancies on the surface *via* the thermal exfoliation route. The as-prepared ultrathin g-C_3N_4 nanosheets display a photocatalytic NH_4^+ production rate of 54 μmol L^{-1} in 100 min in the presence of no co-catalysts or sacrificial reagents, about 2.25 times larger than that of bulk g-C_3N_4. Such an improved activity originates from the carbon vacancies on the surface and ultra-small thickness, which favour the efficient charge carrier dissociation and transfer both in the bulk and on the surface. Wang *et al.*[26] prepared g-C_3N_4
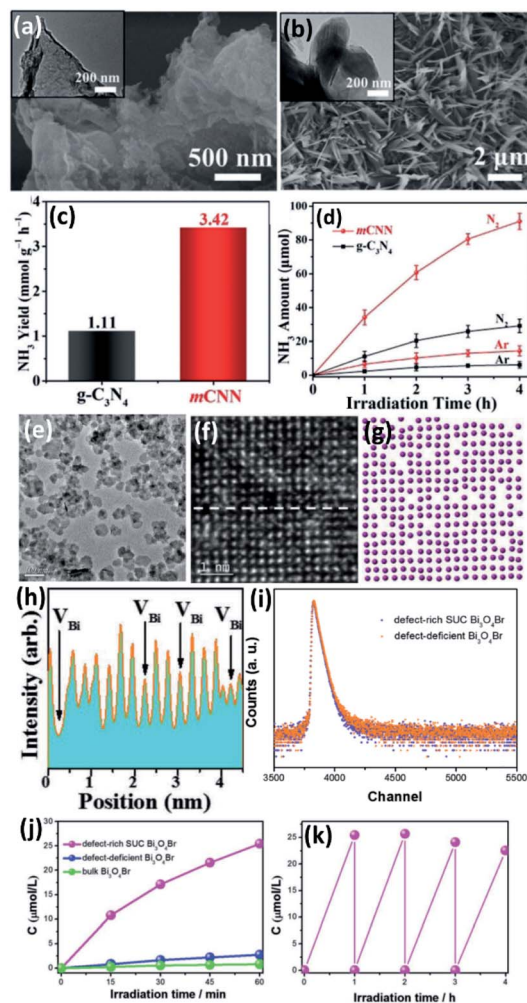

Fig. 1 (a) SEM and TEM (inset) results of pristine g-C_3N_4. (b) SEM and TEM (inset) results of mCNN. (c) Photocatalytic NH_3 production amounts of g-C_3N_4 and mCNN. (d) Photocatalytic NH_3 production amounts *versus* illumination time plots of g-C_3N_4 and mCNN using N_2 and Ar as the feed gases. Reproduced from ref. 26 with permission from John Wiley and Sons. (e) TEM image of Bi_3O_4Br NSs with abundant defects. (f) Atomic-resolution HAADF-STEM images of Bi_3O_4Br NSs with abundant defects; the image has been processed utilizing a Gaussian filter to eliminate noise. (g) Structural model displaying Bi defects on the surface in (f). (h) Line profiles of Bi_3O_4Br NSs with abundant defects. (i) Positron annihilation lifetime spectra of Bi_3O_4Br NSs with abundant defects and Bi_3O_4Br with few defects. (j) Photocatalytic NH_3 production under light illumination. (k) Stability test of photocatalytic NH_3 production of defect-rich Bi_3O_4Br NSs under light illumination. Reproduced from ref. 31 with permission from John Wiley and Sons.

nanoribbons with intercalated K^+ and cyano groups (mCNN). Compared to the scanning electron microscopy (SEM) (see Fig. 1a) and transmission electron microscopy (TEM) (see Fig. 1a inset) images of pristine g-C_3N_4, the SEM (Fig. 1b) and TEM (Fig. 1b inset) images of mCNN display its ribbon-shaped structures with uniform size, due to the scissoring out effect of molten KOH in the preparation process. A visible-light-driven photocatalytic NH_3 production activity of 3.42 mmol g^{-1} h^{-1} was obtained on the as-prepared mCNN, obviously larger than

18736 | *J. Mater. Chem. A*, 2021, **9**, 18733–18745

This journal is © The Royal Society of Chemistry 2021

that on pristine g-C_3N_4 (1.11 mmol g^{-1} h^{-1}) as displayed in Fig. 1c. Fig. 1d presents the photocatalytic NH_3 production amounts of pristine g-C_3N_4 and mCNN photocatalysts utilizing N_2 or Ar as the feed gas. As Ar was utilized as the feed gas without N_2, pristine g-C_3N_4 and mCNN photocatalysts present average photocatalytic NH_3 production activities of 0.23 and 0.52 mmol g^{-1} h^{-1}, respectively. These results indicate that the nitrogen source of the produced NH_3 arises from photocatalysts, as Ar is utilized as the feed gas. Both experiments and theoretical computations support that the cyano group in mCNN is regenerated with the assistance of intercalated K^+, similar to the Mars–van Krevelen process. The regeneration of the cyano group results in the improved activity and stability of mCNN. In another study, g-C_3N_4 porous nanosheets with doped sulphur and carbon vacancies (SCNNSs) have been prepared via heating melamine and trithiocyanuric acid together.[27] A photocatalytic NH_3 generation activity of 5.99 mM h^{-1} g^{-1} was acquired on the as-synthesized SCNNSs using simulated sunlight illumination. This activity is 280% times larger than that of bulk S doped g-C_3N_4. It was found that the porous sheet structure, ultra-small thickness, and incorporation of sulphur and carbon vacancies induce better photocatalytic performance.

Apart from the above studies, investigations based on theoretical calculations have been applied to study the g-C_3N_4 photocatalyst for NH_3 production. For instance, Lv et al.[28] utilized density functional theory (DFT) based computations to explore the single B atom loaded on holey graphitic carbon nitride (B@g-CN) towards the photocatalytic nitrogen reduction reaction (NRR). The DFT computation results indicate that efficient N_2-to-NH_3 conversion can be achieved via the enzymatic pathway on B@g-CN with a very low activation barrier of 0.61 eV and overpotential of 0.15 V. These values are lower than those of many metal-based catalysts. Besides, the photo-excited electrons on B@g-CN can sufficiently enable the NRR against the hydrogen evolution reaction (HER). In another study, on the basis of DFT calculation results, Ren et al.[29] found that nitrogen vacancies not only boost the dissociation of photo-excited electron–hole pairs in g-C_3N_4, but also increase the light absorption. Besides, they also found that the corrugated configuration structure of g-C_3N_4 favours the N_2 adsorption ability, thus improving the photocatalytic N_2 fixation activity.

3.2 Bismuth based 2D photocatalysts

Due to the fascinating features of adjustable light-harvesting ability, internal electric field, easy creation of surface oxygen vacancy and photochemical stability, 2D Bi-based photocatalysts have drawn tremendous attention recently.[30–32] Different 2D Bi-based photocatalysts, e.g., BiOCl,[30] Bi_3O_4Br[31] and BiOBr,[32] were prepared and adopted for photocatalytic NH_3 production. For example, Wu et al.[30] prepared Br doped BiOCl micro-sheets with abundant O vacancies and exposed {001} facets (Br–BiOCl–OV) using a surfactant assisted solvothermal approach and a subsequent ion-exchange method. An NH_3 production activity of 6.3 μmol h^{-1} was achieved on the optimized Br–BiOCl–OV utilizing visible light, ca. 150% larger than

that of bare BiOCl. The incorporation of the Br ion not only leads to a better N_2 activation effect based on theoretical calculations, but also narrows the band gap width as well as raising the conduction band position, resulting in enhanced light absorption and stronger reduction capacity. Besides, Br–BiOCl–OV also presents improved dissociation of photo-induced excitons. The aforementioned effects synergistically cause the elevated photocatalytic NH_3 generation rate of Br–BiOCl–OV.

Di et al.[31] synthesized single-unit-cell (SUC) Bi_3O_4Br nanosheets with confined defects using a polyvinylpyrrolidone (PVP) self-assembly approach. The TEM image of SUC Bi_3O_4Br nanosheets is displayed in Fig. 1e, confirming their 2D ultrathin nanosheet structure. Abundant point defects are observed on SUC Bi_3O_4Br nanosheets as shown in the aberration-corrected atomic-resolution high angle annular dark field scanning transmission electron microscopy (HAADF-STEM) image (Fig. 1f). The structure model in Fig. 1g presents the surface point defects in Fig. 1f. Accordingly, the line profiles in Fig. 1h indicate that the numerous point vacancies correspond to Bi vacancies confined in SUC Bi_3O_4Br NSs. The presence of Bi vacancy can significantly increase the production of oxygen vacancies as confirmed by both theoretical computations and experimental results. Fig. 1i exhibits the positron annihilation lifetime spectra of SUC Bi_3O_4Br NSs with abundant defects and Bi_3O_4Br with few defects. The acquired positron annihilation lifetime parameters indicate the higher concentration of Bi surface defects in defect-rich SUC Bi_3O_4Br NSs compared with that of defect-deficient Bi_3O_4Br NSs. As displayed in Fig. 1j, after one-hour reaction, the defect-rich SUC Bi_3O_4Br NSs exhibit a larger amount of NH_3 (25.4 μmol L^{-1}) in a N_2 atmosphere, about 9.2 and 30.9 times larger than that of Bi_3O_4Br NSs with deficient defects and bulk Bi_3O_4Br, respectively. Besides, no apparent decrease of the photocatalytic NH_3 production activity is observed after four cycles (Fig. 1k), suggesting the good stability of defect-rich SUC Bi_3O_4Br NSs. The enhanced photocatalytic NH_3 production performance arises from the efficient dissociation and transportation of photo-excited electrons and holes, owing to their SUC configuration and surface defects. Moreover, Xue et al.[32] fabricated oxygen vacancy engineered BiOBr ultrathin NSs mainly exposed with {001} crystal facets through utilizing PVP in the hydrothermal procedure. The BiOBr ultrathin NSs with oxygen vacancies exhibit about 10 times larger photocatalytic NH_3 production rate (54.70 μmol g^{-1} h^{-1}) compared to BiOBr nanoplates in the absence of any oxygen vacancies (5.75 μmol g^{-1} h^{-1}). They found that the engineering of oxygen vacancies in BiOBr ultrathin NSs not only reduces the band gap and strengthens the light harvesting, but also raises the conduction band position for stronger reduction capability of photo-induced electrons. Besides, both the experiments and theoretical computations indicate that the adsorption and activation of N_2 molecules could be promoted by oxygen vacancies.

3.3 LDH based 2D photocatalysts

As a novel category of metal-to-metal charge-transfer (MMCT) based system, LDHs are highly promising in the photocatalysis

This journal is © The Royal Society of Chemistry 2021

J. Mater. Chem. A, 2021, **9**, 18733–18745 | **18737**

field, owing to their adjustable metal cation components and tailorable thickness combined with engineering of defects and band structures.[33] Thus, a range of LDH based photocatalysts have been developed.[33–35] For instance, Zhao et al.[34] reported the fabrication of LDH NSs (i.e., ZnCr–LDH, ZnAl–LDH and NiAl–LDH) with plentiful O vacancies, cation vacancies and coordinatively unsaturated metal sites via an alkali-etching process. All the alkali-etched LDH NSs exhibit superior photocatalytic NH_3 production activities compared to their un-etched counterparts. In particular, etched ZnCr–LDH presents a photocatalytic NH_3 production activity of 33.19 μmol g^{-1} h^{-1} with an apparent quantum efficiency (AQE) of 0.11% at 550 nm, ca. 1000% times larger in contrast to that of un-etched ZnCr–LDH (3.15 μmol g^{-1} h^{-1}). The alkali-etching approach not only elevates the conduction band edge of ZnCr–LDH to improve the reduction capacity of photo-induced electrons, but also reduces its band gap for stronger absorption of visible light. Besides, the alkali-etching approach generated vacancies in ZnCr–LDH, which act as trapping centres for photo-induced electrons and elongate the charge-carrier lifetimes. Moreover, the unsaturated Zn sites created by the alkali-etching method further favour the adsorption and activation of N_2. Hence, boosted photocatalytic NH_3 production activities are achieved on the etched ZnCr–LDH. In another report, a facile co-precipitation method was employed to synthesize a range of $M^{II}M^{III}$ (M^{II} = Mg, Zn, Ni, Cu; M^{III} = Al, Cr) LDH ultrathin NSs.[33] Fig. 2a and b show the TEM images of CuCr LDH ultrathin NSs, suggesting their NS structure with an averaged lateral size of about 20 nm and a thickness of approximately 2.5 nm. The high-resolution (HR)-TEM image of CuCr LDH ultrathin NSs (Fig. 2c) displays a d spacing of 0.24 nm, ascribed to the (009) facet of CuCr LDH ultrathin NSs. As presented in Fig. 2d, the averaged length of the first Cr–O shell within CuCr-NS is 1.989 Å, smaller than that acquired within CuCr-bulk. Furthermore, the Cr in CuCr-NS shows a decreased coordination number of 5.5, in comparison to the Cr in CuCr-bulk (6.0). This result suggests a seriously distorted structure around Cr cations within CuCr-NS, in agreement with the presence of plentiful oxygen vacancies. Fig. 2e shows the explanation of the in-plane compressive strain caused by the abundant oxygen vacancies. As presented in Fig. 2f, many LDH NSs exhibit photocatalytic NH_3 production activities utilizing visible light (λ > 400 nm). Particularly, CuCr–LDH NSs display the highest photocatalytic NH_3 generation rate of 142.9 μmol L^{-1}. Additionally, an apparent quantum yield (AQY) of 0.10% at 500 nm was also obtained on CuCr–LDH NSs. To study the adsorption/activation/reduction of N_2, in situ diffuse reflectance infrared Fourier transform spectroscopy was adopted to probe the reaction intermediates on the CuCr–LDH NS surface (Fig. 2g). The characteristic bands at 1661, 1557 and 1448 cm^{-1} correspond to the antisymmetric as well as symmetric deformations of surface NH_4^+ species. Both the adsorption/activation of N_2 and H_2O molecules are promoted via the abundant O vacancies in CuCr–LDH NSs. In addition, the structure distortions and compressive strain caused by the incorporation of Cu^{2+} also result in enhanced interaction between N_2 and LDH, thus increasing NH_3 production. Furthermore, Zhang et al.[35] have prepared ZnAl–LDH NS with incorporated Cu^{2+} and

Fig. 2 (a and b) TEM and (c) HRTEM results of CuCr-NS. (d) Magnitude of k^2-weighted FT of Cr K-edge EXAFS spectra of CuCr-bulk and CuCr-NS. (e) Explanation of the in-plane biaxial compressive strain in the as-prepared LDH nanosheets. (f) Photocatalytic NH_3 production amount of various LDH photocatalysts using visible-light irradiation (λ > 400 nm). (g) In situ IR spectra collected on CuCr-NS in the process of 125 min UV-vis irradiation in a N_2 and water vapor atmosphere. Reproduced from ref. 33 with permission from John Wiley and Sons. (h) Magnitude of k^2-weighted FT of Ti K-edge EXAFS spectra for X%-TiO_2 NS (X = 0, 1, 3, 6, 8) and bulk-TiO_2 NSs; the inset in (h) displays the amplified view of the Ti−O signal. (i) 2D structure model for TiO_2 NSs with oxygen vacancies and engineered strain. (j) Photocatalytic NH_3 production amounts for various samples using water as the proton source after 1 hour UV-vis illumination; the produced NH_3 was detected using Nessler's reagent. (k) Time course of photocatalytic NH_3 production on 6%-TiO_2 utilizing 600 nm and 700 nm illumination; the produced NH_3 was detected by ion chromatography. Reproduced from ref. 36 with permission from John Wiley and Sons.

plentiful oxygen vacancies utilizing an easy co-precipitation route. The Cu modified ZnAl–LDH NS exhibits an outstanding photocatalytic NH_3 production activity of 110 μmol g^{-1} h^{-1} in pure water using UV-visible illumination. Excellent robustness in photocatalytic NH_3 production was also found on this Cu modified ZnAl–LDH NS. Its outstanding photocatalytic performance arises from the presence of numerous oxygen vacancies

18738 | J. Mater. Chem. A, 2021, 9, 18733–18745

This journal is © The Royal Society of Chemistry 2021

and electron-rich $Cu^{\delta+}$ advancing the N_2 adsorption/activation as well as electron–hole dissociation and transportation.

3.4 Other 2D photocatalysts

Apart from the above-mentioned 2D photocatalysts, other 2D photocatalysts, such as TiO_2 NSs,[36] MoO_{3-x} nanobelts,[37] ultrathin MoS_2 NSs[38] and amorphous SmOCl NSs,[39] have also been explored for photocatalytic NH_3 generation. For example, Zhao et al.[36] doped copper in TiO_2 NSs for producing more oxygen vacancies and massive compressive strain. X-ray absorption fine structure (XAFS) was adopted to study the local atomic structure and cation coordination in X%-TiO_2 ($X = 0, 1, 3, 6, 8$) resulting from Cu incorporation in the TiO_2 NSs. Fig. 2h presents the magnitude of k^2-weighted Fourier transforms of Ti K-edge EXAFS for X%-TiO_2 ($X = 0, 1, 3, 6, 8$) and bulk-TiO_2. It is observed that the Ti–O shell peak intensity is increasingly lowered upon the increase of Cu concentration in TiO_2 from 0% to 6%, in agreement with the increase of O vacancies. Fig. 2i demonstrates the strain caused by the O vacancies and Jahn–Teller effect arising from the incorporation of Cu. As can be seen from Fig. 2j, 6%-TiO_2 presents the largest photocatalytic NH_3 generation activity of 78.9 μmol g^{-1} h^{-1} among various samples. Besides, Fig. 2k shows that no NH_3 was produced in an Ar atmosphere using 600 nm and 700 nm illumination. In contrast, in a N_2 flow, the concentration of generated NH_3 rises linearly with the illumination time. 6%-TiO_2 exhibits photocatalytic NH_3 production activities of 1.54 and 0.72 μmol g^{-1} h^{-1} utilizing 600 nm and 700 nm illumination, respectively. Moreover, 6%-TiO_2 shows the excellent reliability of photocatalytic NH_3 production in 5 cycles of testing. The outstanding photocatalytic NH_3 production performance is ascribed to the ample oxygen vacancies and compressive strain arising from the Jahn–Teller distortion via doping Cu, which are supported by a series of characterization techniques, e.g., X-ray diffraction (XRD), XAFS and electron paramagnetic resonance (EPR) spectroscopy, together with theoretical calculations. Moreover, the preparation of oxygen vacancy-rich MoO_{3-x} nanobelts was accomplished through adopting a hydrothermal approach.[37] The oxygen vacancies are found on the (001) and (100) crystal facets of MoO_{3-x} nanobelts confirmed by the scanning transmission electron microscopy (STEM) characterizations results. Efficient photocatalytic generation of NH_3 via N_2 reduction was realized on oxygen vacancy-rich MoO_{3-x} nanobelts, thanks to the existence of oxygen vacancies benefiting the chemisorption/activation of N_2 molecules.

The preparation of ultrathin MoS_2 using a hydrothermal method was presented by Sun et al.[38] The ultrathin MoS_2 exhibits a photocatalytic NH_3 generation activity of 325 μmol h^{-1} g^{-1} utilizing no electron donor or co-catalyst. This excellent photocatalytic activity of ultrathin MoS_2 arises from the light-induced trions activating and converting N_2 molecules into NH_3 through a simultaneous six-electron reduction procedure.

Hou et al.[39] have prepared amorphous SmOCl nanosheets (A-SmOCl) utilizing graphene oxide (GO) as a template by a wet-chemical approach. The as-fabricated A-SmOCl displays a photocatalytic NH_3 generation rate of 426 μmol h^{-1} g^{-1} under

xenon light illumination (320–780 nm), with an AQY efficiency of 0.32% at 420 nm. Its impressive photocatalytic activity is ascribed to the presence of plentiful O vacancies in A-SmOCl enhancing the N_2 adsorption/activation and increasing the light absorption range. Besides, the O K-edge XAS result corroborates the strengthened Sm–O covalency, which advances the migration of photo-induced electrons to the chemisorbed N_2 molecules, thus increasing the photocatalytic activity of A-SmOCl.

For most single-component 2D photocatalysts discussed in Sections 3.1–3.4, the generation of vacancies (e.g., O vacancies, N vacancies and C vacancies)[24,25,27,30–37,39] is a general and effective strategy to apparently boost the adsorption of N_2 molecules and promote their subsequent activation and reduction. Thus, the light-induced N_2-to-NH_3 conversion performance is greatly enhanced on these single-component 2D photocatalysts engineered with vacancies.

4. 2D material based heterostructured photocatalysts

The unique properties (e.g., large surface area and highly exposed surface atoms) of 2D building blocks benefit their electronic coupling with other materials to achieve efficient interfacial dissociation and transportation of photo-induced charge carriers. In addition, a robust combination can also be achieved to realize high stability in photocatalytic NH_3 production. Hence, various 2D material based heterostructured photocatalysts have been designed and synthesized towards photocatalytic N_2 reduction (see Table 2).[40–51] They can be categorized into 0D/2D binary heterostructures,[40–46] 2D/2D binary heterostructures,[47,48] 3D/2D binary heterostructures[49] and ternary heterostructures.[50,51]

4.1 0D/2D binary heterostructures

0D/2D heterostructured photocatalysts are the most extensively studied binary heterostructured photocatalysts. Based on the intrinsic features of the formed heterojunction, they are classified into metal/semiconductor 0D/2D heterostructures,[40–43] semiconductor/semiconductor 0D/2D heterostructures,[44,45] and semiconductor/semimetal 0D/2D heterostructures.[46]

For instance, Liu et al.[40] anchored single-atom Ru on TiO_2 NS by impregnation and calcination in an Ar–H_2 atmosphere. Both the aberration-corrected HAADF-STEM and synchrotron-based EXAFS spectra confirm the existence of single-atom Ru on the TiO_2 NS surface. The DFT calculations further reveal the largest adsorption energy of the Ru–O–Ru structure in defective TiO_2 with O vacancies, indicating that the formation of O vacancies via thermal H_2 treatment could stabilize the atomic dispersion of Ru on the TiO_2 NS surface. The single-atom Ru anchored TiO_2 NSs exhibit a higher photocatalytic NH_3 production activity (56.3 μg h^{-1} g^{-1}) than unloaded TiO_2 NSs (22.2 μg h^{-1} g^{-1}) utilizing xenon light. This elevated photocatalytic NH_3 production rate arises from the presence of single-atom Ru facilitating the charge separation/migration via accepting the photo-induced electrons into the empty d orbitals as well as

This journal is © The Royal Society of Chemistry 2021

J. Mater. Chem. A, 2021, **9**, 18733–18745 | **18739**

Table 2 Heterostructured 2D photocatalysts for NH$_3$ production

Photocatalyst	Synthesis method	Light source	Reactant solution	NH$_3$ production		Stability	Detection method	References (year)
				Activity (μmol h^{-1} g^{-1})	Quantum efficiency (%)			
0D/2D Ru/TiO$_2$	Impregnation and calcination in H$_2$/Ar	Xe lamp	20 vol% ethanol aqueous solution	ca. 3.3		>2 hours	Indophenol blue method	40 (2019)
0D/2D Cu/g-C$_3$N$_4$	Impregnation and annealing treatment in N$_2$	Xe lamp (780 nm > λ > 420 nm)	20 vol% ethanol aqueous solution	186	1.01 at 420 nm	>3 hours	Nessler's reagent	41 (2018)
0D/2D Au/TiO$_2$	Self-assembly via electrostatic attraction	Xe lamp (λ > 420 nm)	10 vol% methanol aqueous solution	130.5	0.82 at 550 nm	>9 hours	Indophenol blue method	42 (2018)
0D/2D Au/(BiO)$_2$CO$_3$	Hydrothermal method and chemical bath deposition	Xe lamp	Milli-Q water	38.23		<1 hour	Indophenol blue method	43 (2017)
0D/2D AgIn$_2$S$_4$/MXene Ti$_2$C$_3$	Hydrothermal method	Xe lamp (λ > 400 nm)	20 v% methanol aqueous solution	38.8	0.07 at 420 nm	<15 hours	Indophenol blue method	44 (2019)
0D/2D AgCl/δ-Bi$_2$O$_3$	Hydrothermal controllable precipitation approach	Xe lamp (λ > 400 nm)	Deionized water	606		>3 hours	Nessler's reagent	45 (2019)
0D/2D POM/RGO	Stirring at 85 °C using L-ascorbic as the reducing reagent	Xe lamp	Distilled water	130.3 μmol L^{-1} h^{-1}		>1 hour	Nessler's reagent	46 (2019)
2D/2D MoO$_2$/BiOCl	Mechanical mixing	Xe lamp	Deionized water	35		>5 hours	Nessler's reagent	47 (2019)
2D/2D BP/g-C$_3$N$_4$	Ultrasonication, drying and calcination	Xe lamp (λ > 420 nm)	5 vol% methanol aqueous solution	347.5 μmol L^{-1} h^{-1}		>20 hours	Nessler's reagent	48 (2018)
3D/2D PrCO$_3$OH/g-C$_3$N$_4$	Hydrothermal method	Xe lamp	10 vol% methanol aqueous solution	8900		>5 hours	Nessler's reagent	49 (2018)
Ternary MoS$_2$/C-ZnO	Hydrothermal, calcination and photo-deposition	Xe lamp (λ > 420 nm)	5 vol% ethanol aqueous solution	245.7 μmol L^{-1} g^{-1} h^{-1}		>24 hours	Nessler's reagent	50 (2018)
Ternary TiO$_2$@C/g-C$_3$N$_4$	One-step calcination	Xe lamp (λ > 420 nm)	20 vol% methanol aqueous solution	250.6	0.14 at 420 nm	>10 hours	Nessler's reagent	51 (2019)

18740 | J. Mater. Chem. A, 2021, 9, 18733–18745

This journal is © The Royal Society of Chemistry 2021

enhancing the N_2 adsorption and activation. In another study, single-atom Cu anchored g-C_3N_4 was fabricated by Huang et al.[41] The as-prepared Cu loaded g-C_3N_4 displays a photo-catalytic NH_3 generation rate of 186 μmol h^{-1} g^{-1} utilizing visible-light illumination ($\lambda > 420$ nm) and a quantum efficiency of 1.01% at 420 nm. Such an activity is ca. 8 times larger than that of unmodified g-C_3N_4. The improved photocatalytic performance is ascribed to the active isolated π electrons as well as excellent adsorption capacity on the positively charged Cu ions, as corroborated by EXAFS, operando FTIR, operando EPR and theoretical computation results. Moreover, Yang et al.[42] reported the preparation of Au nanosphere loaded TiO_2 ultra-thin nanosheets (UNSs) with oxygen vacancies (Au/TiO_2–OV). Fig. 3a shows that Au nanospheres are uniformly dispersed on the surface of TiO_2 UNSs with O vacancies (TiO_2–OV). The existence of OVs was tested by low-temperature EPR analysis. TiO_2 and Au/TiO_2 exhibit no EPR signals (Fig. 3b). TiO_2–OV and Au/TiO_2–OV display a peculiar OV signal with a g factor of 1.998, indicating the existence of OVs (Fig. 3b). N_2 TPD was applied to analyze the N_2 adsorption ability of all the as-prepared samples. Both TiO_2 and Au/TiO_2 samples merely display an adsorption peak, resulting from N_2 physisorption. In comparison, apart from the physisorption peak, both TiO_2–OV and Au/TiO_2–OV exhibit a peak located at a higher temperature, attributed to the N_2 chemisorption (Fig. 3c). This result indicates that N_2 chemisorption occurs at the OV sites on the TiO_2 NS surface. The electron migration from OV-induced Ti^{3+} and N_2 is deemed to be the major cause of the N_2 chemisorption. As shown in Fig. 3d, Au/TiO_2–OV presents a photocatalytic NH_3 production activity of 78.6 μmol h^{-1} g^{-1}, ca. 98 and 35 times higher than those of Au/TiO_2 and TiO_2–OV, respectively. No noticeable decrease in the photocatalytic NH_3 generation rate of Au/TiO_2–OV is observed over five cycles of testing, suggesting its good stability. Fig. 3e illustrates the photocatalytic NH_3 production mechanism of the Au/TiO_2–OV system. Under light illumination, hot electrons are produced in Au nanospheres and injected into the TiO_2 NS conduction band. Then the hot electrons are trapped in defect states caused by the OV in TiO_2 NSs. Subsequently, the hot electrons reduce the N_2 molecule adsorption and activation at the OV sites. In the meantime, the hot holes in the Au nanospheres are mainly used up by the methanol as an electron donor. This highly efficient "working-in-tandem" photocatalytic mechanism leads to the outstanding NH_3 production performance in the Au/TiO_2–OV system. Furthermore, a chemical bath deposition (CBD) approach was adopted by Xiao et al.[43] to load Au nanoparticles (NPs) on the surface of $(BiO)_2CO_3$ nanodisks (NDs). An improved photocatalytic NH_3 generation activity of 38.23 μmol mg^{-1} h^{-1} was observed on the as-prepared Au NP deposited $(BiO)_2CO_3$ NDs in comparison to that of $(BiO)_2CO_3$ NDs alone. This is because Au NPs can increase light absorption and generate hot electrons for N_2 reduction as well as rapidly accepting the photo-excited electrons and promoting electron–hole separation.

Several semiconductor/semiconductor 0D/2D hetero-junctions have also been developed for photocatalytic NH_3 production.[44,45] For example, 0D AgInS$_2$ NP loaded 2D MXene Ti$_3$C$_2$ NSs were fabricated via in situ growth utilizing

a hydrothermal method.[44] The as-fabricated 0D/2D AgInS$_2$/Ti$_3$C$_2$ heterostructure displays a photocatalytic NH_3 production activity of 38.8 μmol g^{-1} h^{-1} utilizing visible light ($\lambda > 400$ nm) in 20% methanol aqueous solution. An AQE of 0.07% at 420 nm was also achieved on this 0D/2D AgInS$_2$/Ti$_3$C$_2$ heterostructure. The origin of the excellent photocatalytic NH_3-production activity was studied by both experimental characterization and theoretical calculations. The 2D morphology of Ti$_3$C$_2$ NSs and the Z scheme heterostructure formed between AgInS$_2$ and Ti$_3$C$_2$ apparently benefit the photo-induced electron–hole pair disso-ciation as well as movement. The high specific surface area of Ti$_3$C$_2$ NSs with ample surface reactive sites facilitates the adsorption/activation/reduction of N_2. Furthermore, the DFT based theoretical computations also corroborate the sponta-neous activation of N_2 molecules on Ti$_3$C$_2$ NSs via a di-nuclear end-on bound structure. In addition, Gao et al.[45] fabricated a p–n heterojunction of AgCl/δ-Bi$_2$O$_3$ ultrathin NSs by a two-step
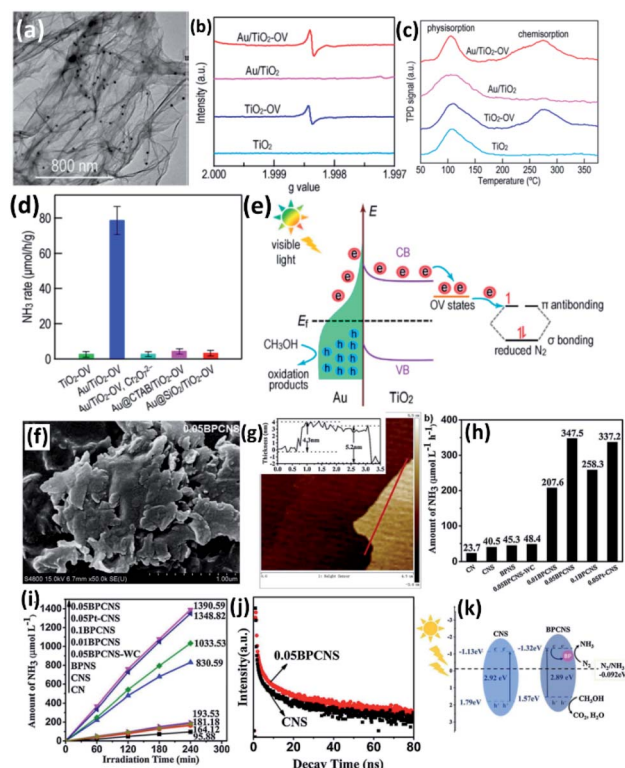
Fig. 3 (a) TEM result of Au/TiO_2–OV. (b) EPR spectra for Au/TiO_2–OV, Au/TiO_2, TiO_2–OV and TiO_2. (c) N_2 TPD profiles for Au/TiO_2–OV, Au/TiO_2, TiO_2–OV and TiO_2. (d) Photocatalytic NH_3 production activities of various samples using visible light irradiation ($\lambda > 420$ nm). (e) Schematic illustration for the production of plasmonic hot electrons in Au NSs, electron transfer into the TiO_2 conduction band, and N_2 reduction in photocatalytic NH_3 production on Au/TiO_2–OV using visible-light illumination ($\lambda > 420$ nm). Reproduced from ref. 42 with permission from the American Chemical Society. (f) SEM and (g) AFM images of 0.05BPCNS. (h) Average photocatalytic NH_3 production activities of various samples in 4 hour reaction. (i) Time course of photocatalytic NH_3 production on various samples. (j) Time-resolved photoluminescence spectra of CNS and 0.05BPCNS. (k) Schematic illustration of the possible photocatalytic mechanism on 0.05BPCNS. Reproduced from ref. 48 with permission from Elsevier.

This journal is © The Royal Society of Chemistry 2021

J. Mater. Chem. A, 2021, **9**, 18733–18745 | **18741**

approach of hydrothermal reaction and precipitation. The AFM characterization indicates a uniform thickness of *ca.* 2.7 nm for the AgCl/δ-Bi$_2$O$_3$ NSs. Both the high-resolution XPS spectra of O 1s and EPR spectrum confirm the presence of oxygen vacancies. The as-prepared AgCl/δ-Bi$_2$O$_3$ NSs present a photocatalytic NH$_3$ generation activity of 606 μmol h^{-1} g^{-1} utilizing visible light (λ > 400 nm), apparently higher than that of δ-Bi$_2$O$_3$ alone. The boosted photocatalytic activity originates from the construction of a p–n heterojunction suppressing the electron–hole recombination and the oxygen vacancies promoting the chemical adsorption/activation of N$_2$. Besides, the ultrathin 2D NS morphology also facilitates the migration of electrons and holes, thus contributing to the improved photocatalytic activity.

Wang *et al.*[46] synthesized three types of polyoxometalates (POMs)/reduced GO composites as semiconductor/semimetal 0D/2D photocatalysts for photocatalytic N$_2$ reduction without any co-catalysts or electron donors. The largest photocatalytic NH$_3$ production activity of 130.3 μmol L^{-1} h^{-1} was obtained on H$_5$[PMo$_{10}$V$_2$O$_{40}$]/reduced graphene oxide. They attribute the excellent performance to three reasons: (i) reduced aggregation of GO with more exposed reactive sites leading to enhanced N$_2$ adsorption; (ii) broad light absorption range and good reduction capacity; and (iii) GO boosting electron migration and inhibiting electron–hole recombination.

4.2 2D/2D binary heterostructures

The integration of two different 2D building blocks to establish a 2D/2D heterostructure is deemed to be an effective strategy because their intimate contact with large interfacial area greatly favours the dissociation and migration of photo-induced electrons and holes as well as strong interaction for achieving excellent stability.[47,48] For instance, Xiao *et al.*[47] have synthesized a 2D/2D MoO$_2$/BiOCl composite *via* electrostatic adsorption. The as-prepared MoO$_2$/BiOCl heterostructure displays an obviously improved photocatalytic activity of 35 μmol g^{-1} h^{-1} for N$_2$ reduction to NH$_3$, compared with either pure MoO$_2$ or bare BiOCl, using xenon light irradiation. They ascribed the improved activity to the presence of MoO$_2$ which not only promoted charge carrier migration but also facilitated the adsorption/activation of N$_2$. Furthermore, Qiu *et al.*[48] combined black phosphorus (BP) NSs with g-C$_3$N$_4$ NSs to form 0.05BPCNS *via* calcination in an Ar atmosphere. The SEM image of 0.05BPCNS displays a rough surface due to the loading of BP NSs (Fig. 3f). The thickness of 0.05BPCNS is shown to be *ca.* 4–5 nm in its AFM image (Fig. 3g). Furthermore, as displayed in Fig. 3h, 0.05BPCNS presents an averaged photocatalytic NH$_3$ generation activity of 347.5 μmol L^{-1} h^{-1}, much larger than that of g-C$_3$N$_4$ NSs (40.5 μmol L^{-1} h^{-1}) or BP NSs (45.3 μmol L^{-1} h^{-1}). The time course of photocatalytic NH$_3$ production of 0.05BPCNS in Fig. 3i confirms its excellent robustness. The XPS characterization results indicate the formation of C–P covalent bonds between g-C$_3$N$_4$ NSs and BP NSs, bringing about improved charge carrier separation/transfer efficiency and increased stability owing to the occupation of lone electron pairs on the P atom. This is also corroborated by the time-resolved photoluminescence spectra (Fig. 3j), which indicate

the longer charge carrier lifetime of 0.05BPCNS compared with that of CNS. The photocatalytic mechanism in Fig. 3k indicates that the photo-induced electrons on the CNS conduction band are transported to BPNS, where the N$_2$ molecules are adsorbed and reduced to form NH$_3$. In the meantime, the photo-induced holes in the CNS valence band oxidize the methanol.

4.3 3D/2D binary heterostructures

Feng *et al.*[49] fabricated a LnCO$_3$OH (Ln = La, Pr) coupled g-C$_3$N$_4$ heterostructure using a hydrothermal approach. Fig. 4a shows the TEM image of the LaCO$_3$OH–CN composite. A hexagonal morphology is observed. Moreover, PrCO$_3$OH with an irregular morphology is dispersed on CN (Fig. 4b). As shown in Fig. 4c, LaCO$_3$OH/g-C$_3$N$_4$ and PrCO$_3$OH/g-C$_3$N$_4$ exhibit improved photocatalytic NH$_3$ generation activities of 8200 and 8900 μmol h^{-1} g^{-1}, respectively. Their activities are much larger than that of g-C$_3$N$_4$ or hydrothermally treated g-C$_3$N$_4$. Besides, both LaCO$_3$-OH/g-C$_3$N$_4$ and PrCO$_3$OH/g-C$_3$N$_4$ display robust stabilities over five cycles of reaction. The XRD and high-resolution XPS spectral results of the used LaCO$_3$OH/g-C$_3$N$_4$ and PrCO$_3$OH/g-C$_3$N$_4$
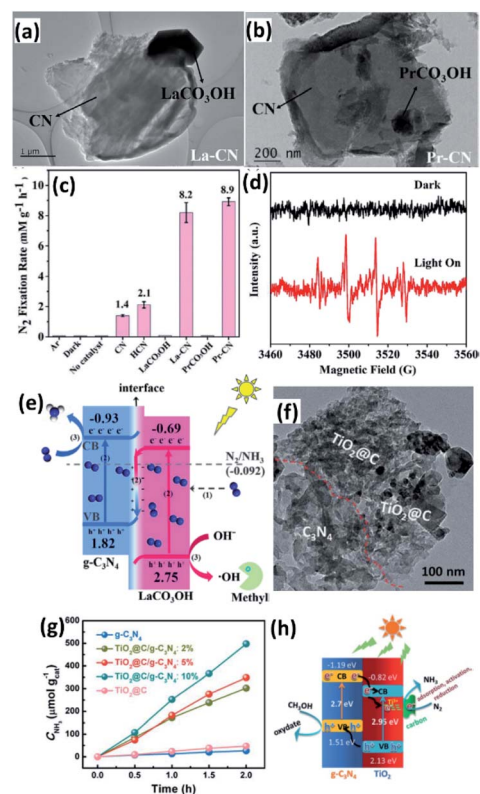

Fig. 4 TEM results of (a) La−CN and (b) Pr−CN. (c) Photocatalytic NH$_3$ production activities of CN, HCN, LaCO$_3$OH, PrCO$_3$OH, La−CN and Pr−CN. (d) The EPR spectra of DMPO−˙OH in the presence of La−CN. (e) The photocatalytic NH$_3$ production mechanism of La−CN. Reproduced from ref. 49 with permission from Elsevier. (f) TEM image of TiO$_2$@C/g-C$_3$N$_4$. (g) Photocatalytic NH$_3$ production activities of various samples using visible light illumination (λ > 420 nm). (h) Schematic illustration for the band alignment and photo-induced electron–hole pair dissociation and migration in the TiO$_2$@C/g-C$_3$N$_4$ system. Reproduced from ref. 51 with permission from RSC.

18742 | *J. Mater. Chem. A*, 2021, **9**, 18733–18745

This journal is © The Royal Society of Chemistry 2021

also confirm the good stabilities of their crystal and chemical structures. Furthermore, the results of the EPR spin-trap test with DMPO in water (Fig. 4d) show four characteristic peaks with an intensity ratio of 1 : 2 : 2 : 1 on LaCO₃OH/g-C₃N₄, ascribed to DMPO–˙OH. Thus, a Z-scheme heterojunction is proposed to form in LaCO₃OH/g-C₃N₄ (Fig. 4e). First, N₂ is adsorbed onto the photocatalysts surface. Upon light illumination, the photo-excited electrons in the LaCO₃OH conduction band recombine with the photo-excited holes in the g-C₃N₄ valence band. The photo-excited electrons on the g-C₃N₄ conduction band reduce the adsorbed N₂ to generate NH₃. Simultaneously, the photo-excited holes on the LaCO₃OH valence band oxidize the OH⁻ to form ˙OH. The formed ˙OH is then captured by methanol as the scavenger. Therefore, they ascribe the excellent photocatalytic NH₃-production performance of LnCO₃OH/g-C₃N₄ to the strong chemical adsorption of N₂ and the efficient electron–hole separation caused by the Z-scheme heterojunction with the Ln–N electron migration channel.

4.4 Ternary heterostructures

2D building blocks have also been applied in complex ternary heterostructured photocatalysts to achieve synergistically enhanced photocatalytic NH₃ generation.[50,51] For example, Xing et al.[50] fabricated a ternary photocatalyst of MoS₂ NP loaded carbon coated ZnO NSs (MoS₂/C–ZnO) via combining hydrothermal and photo-deposition approaches. The optimized 1 wt% MoS₂ loaded carbon coated ZnO (1% MoS₂/C–ZnO) shows the largest photocatalytic NH₃ production activity of 245.7 μmol L⁻¹ g⁻¹ h⁻¹ using simulated sunlight illumination. This activity is 9.3 and 4.0 times larger than that of ZnO and carbon coated ZnO (C–ZnO), respectively. They ascribed the high activity on 1% MoS₂/C–ZnO to the boosted dissociation/migration of charge carriers due to the presence of a carbon layer and MoS₂ as electron trappers. The enlarged surface area also contributes to the improved activity. In contrast, C–ZnO exhibits the largest photocatalytic NH₃ production activity under visible-light irradiation, since the mixed MXene Ti₃C₂Tₓ and melamine was calcined to yield 2D carbon nanosheet-supported TiO₂ NPs wrapped with g-C₃N₄ NSs (TiO₂@C/g-C₃N₄).[51] The TEM image of TiO₂@C/g-C₃N₄ (Fig. 4f) indicates that TiO₂ NPs are dispersed onto the surfaces of C NSs and coupled with g-C₃N₄ NSs. The high-resolution XPS spectrum of Ti 2p confirms the presence of a large amount of Ti³⁺ in TiO₂@C/g-C₃N₄. As presented in Fig. 4g, an excellent visible-light-driven photocatalytic NH₃ generation rate of 250.6 μmol h⁻¹ g⁻¹ accompanied by a quantum yield of 0.14% at 420 nm was obtained on the as-prepared TiO₂@C/g-C₃N₄. This activity is not only ca. 18 and 10 times higher than that of g-C₃N₄ and TiO₂@C, respectively, but also larger than that of a physically mixed TiO₂@C and g-C₃N₄ sample (TiO₂@C + g-C₃N₄). The authors attribute the outstanding activity of TiO₂@C/g-C₃N₄ to its ample surface defects, strong electron-donating capacity, suitable light absorption capability, efficient charge migration and outstanding N₂ activation capacity. Besides, the type II heterostructure established between TiO₂ and g-C₃N₄ also improves the efficient electron–hole dissociation and transportation (Fig. 4h).

For the 2D material based heterostructured photocatalysts discussed in Sections 4.1–4.4, it is of central importance to design and fabricate appropriate heterojunctions (e.g., type II heterojunction, p–n junction and Z scheme) with efficient interfacial charge transfer and a strongly bonded interface to accomplish high activity and stability in photocatalytic NH₃ production. Besides, both reduction and oxidation active sites could be accommodated on different components in the heterojunction on the basis of the migration direction of photo-induced electrons and holes. In particular, the unique advantages of 2D materials, e.g., high surface area, ultrathin thickness and abundant active sites, are greatly beneficial for achieving the above target.

5. Conclusions and outlook

In summary, the design and preparation of single-component and heterostructured photocatalysts using two-dimensional (2D) building blocks are summarized and introduced. The comprehensive and insightful composition/structure–performance relationships in these 2D material based photocatalysts for ammonia production are discussed. The precise and in-depth reaction mechanisms of these 2D material based photocatalysts are also elucidated.

Although some achievements have been made in the above area, there are still many approaches to be developed. For example, it is of great importance to rationally design and fabricate single-component 2D photocatalysts with the following properties: (i) appropriate band gap width for a broad light-responsive range; (ii) desired band edge positions for sufficient redox ability of photo-induced electrons and holes towards the N₂ reduction reaction and oxidation reaction (e.g., water oxidation); (iii) ultrathin thickness and high crystallinity for efficient electron–hole dissociation and transportation; (iv) large surface area and massive active sites (e.g., cation/anion vacancies, doped heteroatoms and specific crystal facets with abundant undercoordinated surface atoms). Apart from the four intriguing above-mentioned properties, the rational design and synthesis of heterostructured 2D material based photocatalysts with the following characteristics is essential: (i) complementary band gap widths of different components in the heterostructures for maximizing the light absorption range; (ii) favourable band alignment (e.g., type II heterojunction, p–n junction and Z scheme heterojunction) for high-efficiency electron–hole separation and transfer; (iii) compatible crystal structures of different components for achieving strong binding, thus facilitating fast interfacial charge migration and high stability; (iv) creation of reduction and oxidation active sites on different components based on the electron–hole transfer direction in the heterojunction.

Furthermore, both state-of-the-art characterization techniques, e.g., aberration-corrected scanning transmission electron microscopy, synchrotron radiation-based X-ray absorption spectroscopy, in situ Fourier transform infrared spectroscopy and in situ Raman, and powerful theoretical calculations can be

This journal is © The Royal Society of Chemistry 2021

J. Mater. Chem. A, 2021, **9**, 18733–18745 | **18743**

combined together to explore the overall and in-depth composition/structure–performance correlation in 2D material based photocatalysts. Besides, a range of newly developed *in situ* or *operando* characterization methods, *e.g.*, *in situ* transmission electron microscopy, *in situ* electron spin resonance spectroscopy, *in situ* Raman and *operando* synchrotron-based X-ray absorption spectroscopy, can be adopted to reveal the actual reaction mechanisms in the photocatalytic ammonia production procedure. The acquired insightful and overall composition–structure/performance relationship, together with the revealed reaction mechanisms will further contribute to the design and preparation of brand-new high-performance photocatalysts utilizing 2D building blocks towards light-driven ammonia generation. Moreover, it is highly promising to adopt powerful theoretical computations for a high-throughput screening of photocatalysts with novel compositions and structures. Then these predicted photocatalysts can be rationally designed and fabricated using advanced nanotechnology to achieve efficient, highly selective and steady light-induced ammonia production.

Conflicts of interest

There are no conflicts to declare.

Acknowledgements

References

1 C. Guo, J. Ran, A. Vasileff and S.-Z. Qiao, *Energy Environ. Sci.*, 2018, **11**, 45.

2 J. Li, H. Li, G. Zhan and L. Zhang, *Acc. Chem. Res.*, 2017, **50**, 112.

3 Z. Wang, X. Hu, Z. Liu, G. Zou, G. Wang and K. Zhang, *ACS Catal.*, 2019, **9**, 10260.

4 X. Chen, N. Li, Z. Kong, W.-J. Ong and X. Zhao, *Mater. Horiz.*, 2018, **5**, 9.

5 K. Ithisuphalap, H. Zhang, L. Guo, Q. Yang, H. Yang and G. Wu, *Small Methods*, 2019, **3**, 1800352.

6 C. Ling, Y. Ouyang, Q. Li, X. Bai, X. Mao, A. Du and J. Wang, *Small Methods*, 2019, **3**, 1800376.

7 X. Yan, D. Liu, H. Cao, F. Hou, J. Liang and S. X. Dou, *Small Methods*, 2019, **3**, 1800501.

8 M. Li, H. Huang, J. Low, C. Gao, R. Long and Y. Xiong, *Small Methods*, 2019, **3**, 1800388.

9 A. J. Medford and M. C. Hatzell, *ACS Catal.*, 2017, **7**, 2624.

10 D. Yan, H. Li, C. Chen, Y. Zou and S. Wang, *Small Methods*, 2019, **3**, 1800331.

11 Y. Zhao, R. Shi, X. Bian, C. Zhou, Y. Zhao, S. Zhang, F. Wu, G. I. N. Waterhouse, L.-Z. Wu, C.-H. Tung and T. Zhang, *Adv. Sci.*, 2019, **6**, 1802109.

12 C. Mao, J. Wang, Y. Zou, H. Li, G. Zhan, J. Li, J. Zhao and L. Zhang, *Green Chem.*, 2019, **21**, 2852.

13 M. Cheng, C. Xiao and Y. Xie, *J. Mater. Chem. A*, 2019, **7**, 19616.

14 Q. Wang, J. Guo and P. Chen, *J. Energy Chem.*, 2019, **36**, 25.

15 M.-H. Vu, M. Sakar, S. A. Hassanzadeh-Tabrizi and T.-O. Do, *Adv. Mater. Interfaces*, 2019, **6**, 1900091.

16 X. Xue, R. Chen, C. Yan, P. Zhao, Y. Hu, W. Zhang, S. Yang and Z. Jin, *Nano Res.*, 2019, **12**, 1229.

17 G. Y. Duan, Y. Ren, Y. Tang, Y. Z. Sun, Y. M. Chen, P. Y. Wan and X. J. Yang, *ChemSusChem*, 2020, **13**, 88.

18 R. Li, *Chin. J. Catal.*, 2018, **39**, 1180.

19 H. Kisch, *Eur. J. Inorg. Chem.*, 2020, 1376.

20 G. Zhang, C. D. Sewell, P. Zhang, H. Mi and Z. Lin, *Nano Energy*, 2020, **71**, 104645.

21 Q. Hao, C. Liu, G. Jia, Y. Wang, H. Arandiyan, W. Wei and B.-J. Ni, *Mater. Horiz.*, 2020, **7**, 1014.

22 J. S. J. Hargreavesa, Y.-M. Chung, W.-S. Ahnc, T. Hisatomid, K. Domen, M. C. Kung and H. H. Kung, *Appl. Catal., A*, 2020, **594**, 117419.

23 Y. Huang, N. Zhang, Z. Wu and X. Xie, *J. Mater. Chem. A*, 2020, **8**, 4978.

24 Y. Xue, Y. Guo, Z. Liang, H. Cui and J. Tian, *J. Colloid Interface Sci.*, 2019, **556**, 206.

25 Y. Zhang, J. Di, P. Ding, J. Zhao, K. Gu, X. Chen, C. Yan, S. Yin, J. Xia and H. Li, *J. Colloid Interface Sci.*, 2019, **553**, 530.

26 W. Wang, H. Zhang, S. Zhang, Y. Liu, G. Wang, C. Sun and H. Zhao, *Angew. Chem., Int. Ed.*, 2019, **58**, 16644.

27 S. Cao, B. Fan, Y. Feng, H. Chen, F. Jiang and X. Wang, *Chem. Eng. J.*, 2018, **353**, 147.

28 X. Lv, W. Wei, F. Li, B. Huang and Y. Dai, *Nano Lett.*, 2019, **19**, 6391.

29 C. Ren, Y. Zhang, Y. Li, Y. Zhang, S. Huang, W. Lin and K. Ding, *J. Phys. Chem. C*, 2019, **123**, 17296.

30 D. Wu, R. Wang, C. Yang, Y. An, H. Lu, H. Wang, K. Cao, Z. Gao, W. Zhang, F. Xu and K. Jiang, *J. Colloid Interface Sci.*, 2019, **556**, 111.

31 J. Di, J. Xia, M. F. Chisholm, J. Zhong, C. Chen, X. Cao, F. Dong, Z. Chi, H. Chen, Y.-X. Weng, J. Xiong, S.-Z. Yang, H. Li, Z. Liu and S. Dai, *Adv. Mater.*, 2019, **31**, 1807576.

32 X. Xue, R. Chen, H. Chen, Y. Hu, Q. Ding, Z. Liu, L. Ma, G. Zhu, W. Zhang, Q. Yu, J. Liu, J. Ma and Z. Jin, *Nano Lett.*, 2018, **18**, 7372.

33 Y. Zhao, Y. Zhao, G. I. N. Waterhouse, L. Zheng, X. Cao, F. Teng, L.-Z. Wu, C.-H. Tung, D. O'Hare and T. Zhang, *Adv. Mater.*, 2017, **29**, 1703828.

34 Y. Zhao, L. Zheng, R. Shi, S. Zhang, X. Bian, F. Wu, X. Cao, G. I. N. Waterhouse and T. Zhang, *Adv. Energy Mater.*, 2020, 2002199.

35 S. Zhang, Y. Zhao, R. Shi, C. Zhou, G. I. N. Waterhouse, L.-Z. Wu, C.-H. Tung and T. Zhang, *Adv. Energy Mater.*, 2020, **10**, 1901973.

36 Y. Zhao, Y. Zhao, R. Shi, B. Wang, G. I. N. Waterhouse, L.-Z. Wu, C.-H. Tung and T. Zhang, *Adv. Mater.*, 2019, **31**, 1806482.

37 Y. Li, X. Chen, M. Zhang, Y. Zhu, W. Ren, Z. Mei, M. Gu and F. Pan, *Catal. Sci. Technol.*, 2019, **9**, 803.

18744 | *J. Mater. Chem. A*, 2021, **9**, 18733–18745

This journal is © The Royal Society of Chemistry 2021

38 S. Sun, X. Li, W. Wang, L. Zhang and X. Sun, *Appl. Catal., B*, 2017, **200**, 323.

39 T. Hou, R. Guo, L. Chen, Y. Xie, J. Guo, W. Zhang, X. Zheng, W. Zhu, X. Tan and L. Wang, *Nano Energy*, 2019, **65**, 104003.

40 S. Liu, Y. Wang, S. Wang, M. You, S. Hong, T.-S. Wu, Y.-L. Soo, Z. Zhao, G. Jiang, J. Qiu, B. Wang and Z. Sun, *ACS Sustainable Chem. Eng.*, 2019, **7**, 6813.

41 P. Huang, W. Liu, Z. He, C. Xiao, T. Yao, Y. Zou, C. Wang, Z. Qi, W. Tong, B. Pan, S. Wei and Y. Xie, *Sci. China: Chem.*, 2018, **61**, 1187.

42 J. Yang, Y. Guo, R. Jiang, F. Qin, H. Zhang, W. Lu, J. Wang and J. C. Yu, *J. Am. Chem. Soc.*, 2018, **140**, 8497.

43 C. Xiao, H. Hu, X. Zhang and D. R. MacFarlane, *ACS Sustainable Chem. Eng.*, 2017, **5**, 10858.

44 J. Qin, X. Hu, X. Li, Z. Yin, B. Liu and K. Lam, *Nano Energy*, 2019, **61**, 27.

45 X. Gao, Y. Shang, L. Liu and F. Fu, *J. Catal.*, 2019, **371**, 71.

46 X.-H. Li, W.-L. Chen, H.-Q. Tan, F.-R. Li, J.-P. Li, Y.-G. Li and E.-B. Wang, *ACS Appl. Mater. Interfaces*, 2019, **11**, 37927.

47 C. Xiao, H. Wang, L. Zhang, S. Sun and W. Wang, *ChemCatChem*, 2019, **11**, 6467.

48 P. Qiu, C. Xu, N. Zhou, H. Chen and F. Jiang, *Appl. Catal., B*, 2018, **221**, 27.

49 X. Feng, H. Chen, F. Jiang and X. Wang, *Chem. Eng. J.*, 2018, **347**, 849.

50 P. Xing, P. Chen, Z. Chen, X. Hu, H. Lin, Y. Wu, L. Zhao and Y. He, *ACS Sustainable Chem. Eng.*, 2018, **6**, 14866.

51 Q. Liu, L. Ai and J. Jiang, *J. Mater. Chem. A*, 2018, **6**, 4102.

52 J. Ran, H. Zhang, J. Qu, J. Shan, S. Chen, F. Yang, R. Zheng, J. Cairney, L. Song, L. Jing and S.-Z. Qiao, *ACS Mater. Lett.*, 2020, **2**, 1484.

53 G. Fiori, F. Bonaccorso, G. Iannaccone, T. Palacios, D. Neumaier, A. Seabaugh, S. K. Banerjee and L. Colombo, *Nat. Nanotechnol.*, 2014, **9**, 768.

54 J. Ran, J. Qu, H. Zhang, T. Wen, H. Wang, S. Chen, L. Song, X. Zhang, L. Jing, R. Zheng and S.-Z. Qiao, *Adv. Energy Mater.*, 2019, **9**, 1803402.

55 J. Ran, H. Wang, H. Jin, C. Ling, X. Zhang, H. Ju, L. Jing, J. Wang, R. Zheng and S.-Z. Qiao, *J. Mater. Chem. A*, 2018, **6**, 23278.

56 J. Ran, B. Zhu and S.-Z. Qiao, *Angew. Chem., Int. Ed.*, 2017, **56**, 10373.

57 T. Carey, S. Cacovich, G. Divitini, J. Ren, A. Mansouri, J. M. Kim, C. Wang, C. Ducati, R. Sordan and F. Torrisi, *Nat. Commun.*, 2017, **8**, 1202.

58 B. Xia, J. Ran, S. Chen, L. Song, X. Zhang, L. Jing and S.-Z. Qiao, *Nanoscale*, 2019, **11**, 8304.

59 J. Ran, G. Gao, F.-T. Li, T.-Y. Ma, A. Du and S.-Z. Qiao, *Nat. Commun.*, 2017, **8**, 13907.

60 J. Ran, X. Wang, B. Zhu and S.-Z. Qiao, *Chem. Commun.*, 2017, **53**, 9882.

61 K. F. Mak and J. Shan, *Nat. Photonics*, 2016, **10**, 216.

62 J. Ran, T. Y. Ma, G. Gao, X.-W. Du and S. Z. Qiao, *Energy Environ. Sci.*, 2015, **8**, 3708.

63 J. Ran, W. Guo, H. Wang, B. Zhu, J. Yu and S.-Z. Qiao, *Adv. Mater.*, 2018, **30**, 1800128.

This journal is © The Royal Society of Chemistry 2021

J. Mater. Chem. A, 2021, **9**, 18733–18745 | **18745**